analytical chemistry

pubs.acs.org/ac Article

Dual-microRNA-Controlled Electrochemiluminescence Biosensor for Breast Cancer Diagnosis and Supplemental Identification of Breast Cancer Metastasis

Zhuoxin Ye, Mo Ma, Yuxuan Chen, Ruiyan Liu, Yan Zhang, Pinyi Ma,* and Daqian Song*

Cite This: *Anal. Chem.* 2024, 96, 3636−3644 Read Online

ACCESS | Metrics & More | Article Recommendations | Supporting Information

ABSTRACT: Breast cancer remains the most frequently diagnosed cancer globally, and the metastasis of this malignancy is the primary cause of mortality in breast cancer patients. Hence, prompt diagnosis and timely detection of metastatic breast cancer are critical for effective therapeutic intervention. Both progression and metastasis of this malignancy are closely associated with aberrant expression of specific microRNAs (miRNAs) and enzymes. To facilitate breast cancer diagnosis and concomitant identification of metastatic breast cancer, we have engineered an innovative electrochemiluminescence (ECL)-based sensing platform integrated with enzyme-free DNA amplification circuits for dual functionality. Specifically, microRNA-21 (miR-21) is employed as a biomarker for breast cancer, and miR-21 induces the quenching of the ECL signal from luminophores via a strategically designed catalytic three-hairpin assembly (CTHA) circuit. Subsequently, miR-105 levels are measured via toehold-mediated strand displacement reactions (TSDR). Here, miR-105 restores the initially quenched ECL signal, enabling the assessment of the metastatic propensity. Our experimental data demonstrate that the devised ECL biosensor offers broad linear detection ranges and low detection limits for both miR-21 and miR-105. Importantly, our novel platform was also successfully validated by using cellular and serum samples. This biosensor not only discriminates breast cancer cell lines MCF-7 and MDA-MB-231 from nonbreast cancer cells like HepG2, TPC-1, and HeLa, but it also distinguishes between malignant MCF-7 and metastatic MDA-MB-231 cells. Consequently, our novel approach holds significant promise for clinical applications and precise cancer screening.

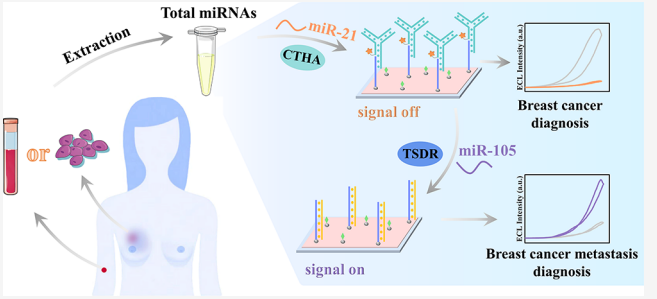

INTRODUCTION

Metastasis continues to be the most significant factor contributing to mortality among cancer patients, severely complicating treatment regimens and prognosis.[1,2] Among the various types of cancer, breast cancer stands out as a particularly prevalent malignancy affecting women globally.[3] Troublingly, approximately 90% of patient deaths related to breast cancer are not due to the primary tumor but are the result of complications arising from recurrent or metastatic disease. These secondary malignancies often remain undetected until they have progressed to advanced stages, making them far more challenging to manage.[4−6] Thus, there is an urgent necessity to identify novel biomarkers and develop advanced detection methodologies for the early stage diagnosis of metastatic breast cancer.

Recent studies provide evidence that microRNAs (miRNAs) act as key mediators in the intricate dialogues between cancer cells and their host.[7−9] Notably, research conducted by Zhou et al. demonstrated that miR-105 is typically expressed in metastatic breast cancer cells, where it facilitates cancer cell migration by disrupting the host's vascular endothelial barriers through targeting the tight junction protein ZO-1. Elevated circulating levels of miR-105 can even be detected in the premetastatic stage, underscoring its potential as both a metastatic biomarker and a therapeutic target.[10,11] However, relying solely on a single biomarker for an early stage diagnosis can lead to inconclusive or misleading results. In contrast, a multibiomarker approach significantly augments the reliability of diagnostic procedures.[12−17] MiR-21 is a well-established biomarker for breast cancer.[18−20] Hence, the concomitant detection of miR-21 and miR-105 not only enhances the specificity and accuracy of early stage breast cancer diagnosis but also holds a prognostic value in determining the likelihood of metastatic progression. Typical multitarget detection platforms usually require multisignal probes to generate fluorescent signals at different wavelengths or electrochemical signals at different potentials.[21−23] Han and co-workers

Received: December 18, 2023
Revised: February 2, 2024
Accepted: February 7, 2024
Published: February 15, 2024

https://doi.org/10.1021/acs.analchem.3c05766
Anal. Chem. 2024, 96, 3636−3644

constructed a potential resolved biosensor for the multicomponent detection of two antigens on cell surfaces.[24] However, anchoring multiple types of probes on the surface of space-limited platforms tends to reduce the utilization efficiency of the capture probes. Therefore, it is urgent to use a single-signal probe and luminescent material for the detection of multiple biomarkers. Yuan's group reported a biosensor based on a dual-miRNA-powered bidirectional DNA walking machine and a biosensor based on a DNA nanogear driven by dual miRNAs,[25,26] and Yang's group constructed a cascade platform for dual-input modulated "and" logic circuits,[21] which are both capable of detecting multiple miRNAs. However, these studies have the following shortcomings: (1) the targets were not amplified; (2) only biomarkers for a single disease were tested, and the development of this disease was not analyzed. Therefore, it is necessary to design a dual-miRNA-controlled biosensor with high sensitivity, high accuracy, high utilization efficiency, and more clinical diagnostic value.

Nevertheless, the detection of miRNA expression levels, although crucial for early diagnosis, faces significant challenges because of their low abundance, small size, and high homology.[27−29] Recently, electrochemiluminescence (ECL) has been widely applied in clinical diagnosis due to its advantages including low cost, robust controllability, and high sensitivity, making it possible to detect miRNA at extremely low levels.[21,30−36] Despite this, ECL assays lack inherent target amplification capabilities. While several enzyme-assisted nucleic acid amplification strategies exist, their application is often limited by an inherent inefficiency stemming from enzyme activities and variable reaction conditions.[29,37−40] Conventional enzyme-based signal amplification strategies are difficult to apply in complex biological systems. This necessitates the use of enzyme-free amplification nucleic acid strategies with high stability and efficiency. Catalytic hairpin assembly (CHA)[41−44] and strand displacement reactions (SDR)[45−47] based on the principles of target triggering and toehold exchange are often applied for the detection of various bioactive molecules. These two strategies are low cost, easy to construct, and less susceptible to environmental interference compared to enzyme-mediated strategies, and both enable cyclic amplification of the target.

Based on the above considerations, this study aims to construct an ECL biosensor capable of simultaneously detecting two critical biomarkers, miR-21 and miR-105, by leveraging enzyme-free DNA amplification circuits. Specifically, we utilized platinum nanoparticle-loaded rubrene nanorods (PtNPs@RubNRs) as the core platform to enhance ECL signals. Furthermore, we implemented two different assembly circuits, namely, the catalytic three hairpin assembly (CTHA) for miR-21 and toehold-mediated strand displacement reactions (TSDR) for miR-105, to achieve a reliable and sensitive detection method. The resulting biosensor amalgamates enzyme-free DNA amplification techniques with ECL technology, presenting an innovative avenue for improving the clinical diagnosis and management of breast cancer.

EXPERIMENTAL SECTIONS

Materials and Reagents. See the Supporting Information.

Preparation of PtNPs@RubNRs. Rubrene nanorods (RubNRs) were synthesized by employing the classical surfactant-assisted reprecipitation method with slight modifications.[48−50] First, 5 mg of rubrene (Rub) powder was dissolved in 5 mL of tetrahydrofuran (THF). The mixture was then sonicated for 5 min to prepare a homogeneous Rub solution. Next, a poly(vinyl alcohol) (PVA) aqueous solution was obtained by mixing PVA powder (83 mg) with 16 mL of deionized water at 60 °C under stirring. The Rub solution was then rapidly injected into the PVA aqueous solution while being stirred vigorously with a stirring paddle (for 15 min total). RubNRs were collected by centrifugation and then washed several times with deionized water.

Subsequently, the composite PtNPs@RubNRs were prepared by *in situ* reduction of platinum nanoparticles (PtNPs) on the surface of RubNRs.[51,52] First, 210 μL of a H_2PtCl_6 aqueous solution (1%) was mixed with 15 mL of RubNRs and stirred for 60 min. Next, 120 μL of a freshly prepared ice-cold $NaBH_4$ (50 mM) solution was added (under vigorous stirring) to the above suspension. The color of the resulting solution was observed to rapidly change from orange to clay. After centrifugation, the precipitate was redispersed in 9 mL of PVA solution containing 230 μL of H_2PtCl_6 (1%) aqueous solution. Under continuous agitation, 120 μL of ascorbic acid (1 M) was injected into the above solution, and the mixture was stirred overnight to induce the formation of PtNPs. PtNPs@RubNRs precipitation products were subsequently obtained by centrifugation and then washed with deionized water. Finally, the products were redispersed into deionized water and stored in a refrigerator at 4 °C away from light.

Assembly of CTHA and TSDR Amplification Circuits. To facilitate self-assembly of the Y-shaped DNA structures of CTHA, H1, H2, and H3 were first heated to 95 °C for 10 min and then slowly cooled to 25 °C to allow the formation of hairpin structures. Different concentrations of target miRNA-21 and hairpins H1, H2, and H3 (final concentrations of 2 μM) were subsequently kept at 37 °C for 3 h to form the stable Y-shaped structures used in later experiments.[42,53]

TSDR assembly was performed as follows. First, L, S, and T (3 μM each in a mixed solution) were annealed at 95 °C for 10 min and then slowly cooled to room temperature to allow hybridization into the L−S−T complex. Next, different concentrations of target miRNA-105 and fuel strand (F) were reacted with L−S−T at 37 °C for 2 h. Ultimately, the product containing strand S was stored in a refrigerator at 4 °C until further use.[46]

Validation of Amplification Circuits by Polyacrylamide Gel Electrophoresis (PAGE). Formation of Y-shaped DNA structures was verified by PAGE. All DNA samples were first mixed with loading buffer (volume ratio 5:1) and then loaded onto a 12% polyacrylamide gel. Electrophoresis was performed at 120 V for 1 h. Likewise, the formation of the TSDR product was confirmed by electrophoresis on a 16% polyacrylamide gel (120 V for 80 min). The gels were stained with Stains-All and the lanes appeared after the gel faded to analyze the results.

Biosensor Fabrication. A bare glassy carbon electrode (GCE) was sequentially polished with 0.3 and 0.05 μm alumina powder and then sonicated in ethanol and ultrapure water to obtain a clean mirror-like electrode.[54] Next, 10 μL of 7-fold diluted PtNPs@RubNRs solution was dropped onto the GCE interface and dried at 37 °C to obtain PtNPs@RubNRs/GCE. After that, 8 μL of sulfhydryl-modified AP (1 μM, treated with TCEP[55]) was incubated on the electrode at 37 °C for 2 h. Followed by rinsing with deionized water, 10 μL of 1 μM hexanethiol (HT) solution was dropped onto the modified electrode. This mixture was then incubated at room temper-

https://doi.org/10.1021/acs.analchem.3c05766
Anal. Chem. 2024, 96, 3636−3644

Scheme 1. Schematic Illustration of the Designed ECL Biosensor[a]

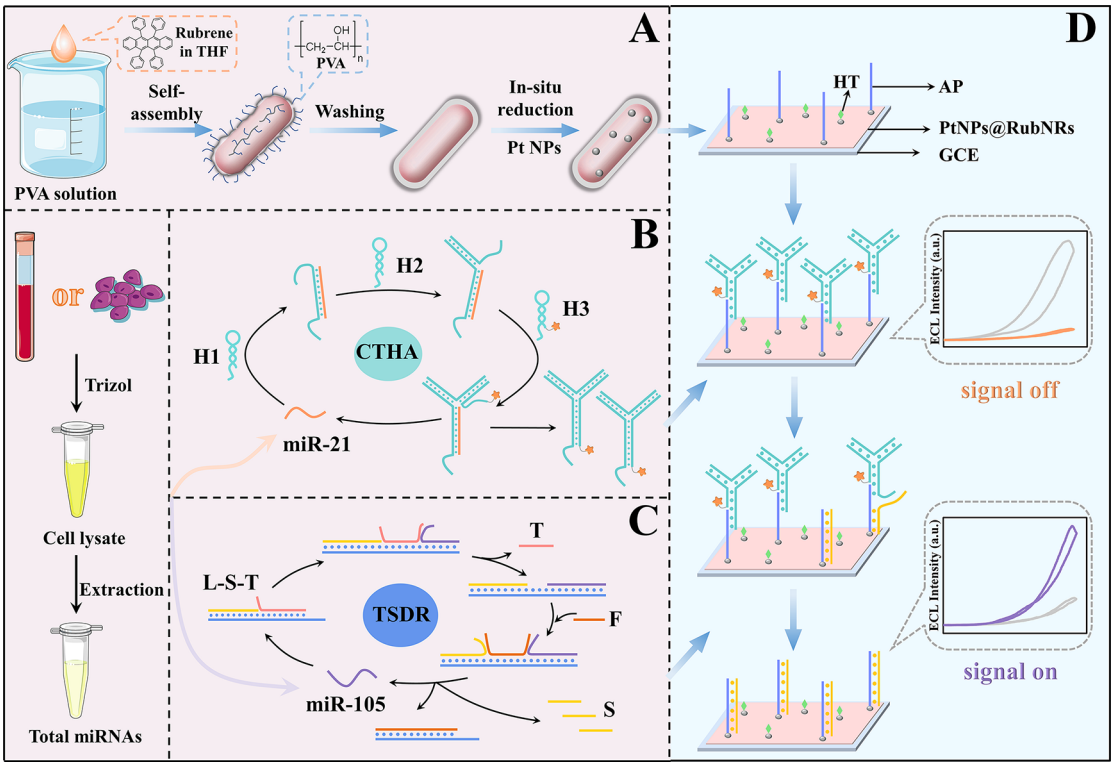

[a](A) Synthesis of PtNPs@RubNRs. (B) miR-21-triggered CTHA amplification circuit. (C) miR-105-triggered TSDR amplification circuit. (D) ECL biosensor assembly process.

ature for 40 min to block nonspecific sites. Subsequent experiments were performed using this ECL biosensing platform (HT/AP/PtNPs@RubNRs/GCE).

ECL Measurement Procedures. Quantitative detection of miR-21 was achieved by measuring the ECL quenching signal. Briefly, CTHA products (8 μL) formed by using different concentrations of miR-21 were dropped onto the modified electrode. The electrode was then incubated at 37 °C for 2 h to allow ferrocene (Fc)-modified Y-shaped structures to hybridize with AP (Y-shaped structures/HT/AP/PtNPs@RubNRs/GCE). After the slurry was rinsed, an ECL signal was recorded from the modified electrodes.

Next, a fixed concentration of miR-21 (the highest concentration of the linear curve) was used to synthesize the Y-shaped structure, which was then dropped onto the modified electrode (HT/AP/PtNPs@RubNRs/GCE). The corresponding ECL signal was used as a known constant in subsequent miR-105 detection experiments. In these experiments, TSDR products (8 μL, containing S) formed using different concentrations of miR-105 were dropped onto the modified electrodes mentioned above (Y-shaped structures/HT/AP/PtNPs@RubNRs/GCE). During incubation of the electrodes at 37 °C for 100 min, free S strands push the Fc-modified Y-shaped structures away from the electrode. After rinsing, ECL data was recorded on the modified electrodes. The ECL signals were measured by using an MPI-E ECL analyzer in 2 mL of 0.1 M phosphatic buffer saline (PBS) solution. This analyzer was used with a scanning rate of 300 mV/s (photomultiplier high voltage of 800 V, amplitude 4) and a potential setting of −0.9 to 1.1 V.

RESULTS AND DISCUSSION

Design Principles of a Novel ECL Biosensor for miR-21 and miR-105 Detection. Scheme 1 outlines the specific design principles of the proposed ECL biosensor for miR-21 and miR-105 detection. First, PtNPs@RubNRs were prepared by the self-assembly method and then employed to construct the ECL biosensing platform (Scheme 1A). The PtNPs acted as coreaction accelerators that promote the reaction rate between RubNRs and dissolved O_2, achieving significant ECL signals ("signal on" state). Next, target-triggered CTHA circuit was performed to form Y-shaped DNA structures for miR-21 detection. The CTHA circuit are formed from three functional hairpins, H1, H2, and H3. To quench the ECL signal, hairpin H3 is modified with Fc.[56] Here, these hairpin reactants remain intact in the absence of miR-21 because their cross-interactions are significantly hindered by intramolecular hybridization. In the presence of miR-21, H1 can be specifically activated, and the CTHA circuit is initiated, resulting in the formation of Y-shaped DNA structures with Fc (Scheme 1B). Importantly, miR-21 is squeezed out to re-enter the CTHA circuit. Thus, a large number of Y-shaped structures are generated. These quench the ECL signal through hybridization with a capture probe (AP) modified on the electrode ("signal off" state). After quantitatively detecting miR-21, it is taken as a known constant to be added to the system during subsequent detection of miR-105. MiR-105 amplification is achieved using a TSDR circuit based on changes in the free energy and the principle of toehold exchange (Scheme 1C). In the presence of miR-105, the TSDR circuit is initiated by miR-105 binding to the toehold of the complex (L−S−T). Ultimately, the TSDR circuit outputs a large number of simulated target S strands

https://doi.org/10.1021/acs.analchem.3c05766
Anal. Chem. 2024, 96, 3636−3644

and miR-105. The extruded miR-105 subsequently triggers a new TSDR circuit cycle. Because S and AP hybridize with high stability, the Y-shaped structure is excluded from the electrode, leading to signal recovery ("signal on" state). In summary, miR-21 causes the biosensor ECL signal to be quenched (an "on−off" switch), and this can be used to diagnose breast cancer. MiR-105 can restore the quenched ECL signal (an "off-on" switch), thus determining whether breast cancer metastasis has occurred.

Structural and Luminescent Characterization of the Rubrene Nanomaterials. Scanning electron microscopy (SEM) was used to observe the morphology of the synthesized Rub nanomaterials. As shown in Figure 1A, PVA-coated

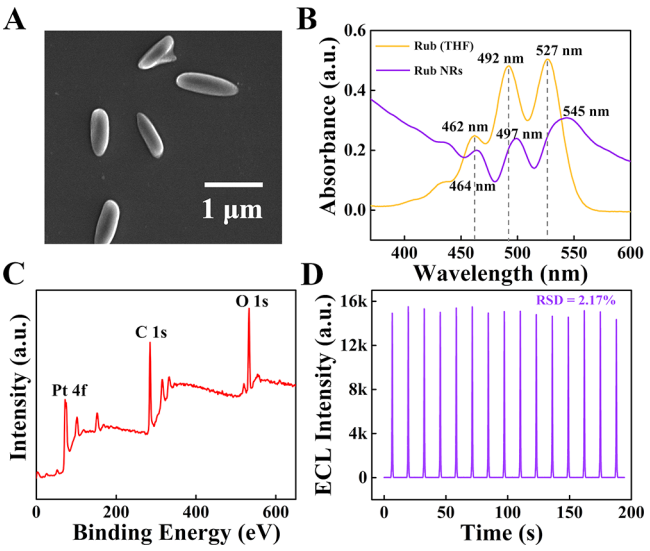

Figure 1. Structural and luminescent characterization of the rubrene nanomaterials. (A) SEM image of RubNRs at a 1 μm scale. (B) UV−vis absorption spectra of Rub (THF) and RubNRs. (C) XPS characterization for the full region of PtNPs@RubNRs. (D) Stability of PtNPs@RubNRs after 15 cycles of continuous scanning.

RubNRs prepared by the reprecipitation method exhibited a uniform rod-shaped structure of length ∼800 nm and width ∼300 nm. The assembly of Rub was further characterized by UV−vis spectroscopy (Figure 1B). The UV−vis absorption spectrum of Rub in THF exhibited three peaks at 462, 492, and 527 nm, consistent with previous reports, indicating the monodisperse state of Rub molecules. However, the UV−vis absorption spectra of the prepared RubNRs showed a slight bathochromic shift, with absorption peaks occurring at 464, 497, and 545 nm, respectively, implying that the Rub molecules aggregated into nanoparticles (J-aggregates).[57] Compared with pure RubNRs, *in situ* reduction of PtNPs on the surface of RubNRs is shown in Figure S4 (Supporting Information). The growth of PdNPs on the RubNRs surface can be clearly observed.

The constituent elements in PtNPs@RubNRs were analyzed by X-ray photoelectron spectroscopy (XPS). As shown in Figure 1C, the characteristic peaks of O 1s, C 1s, and Pt 4f were observed in the PtNPs@RubNRs XPS spectra. The peaks at 532.7 and 284.8 eV in Figure S5 (Supporting Information) belong to O 1s and C 1s, respectively, indicating the presence of Rub and PVA. The XPS doublet of Pt 4f (71.6 and 75 eV) provides evidence that metallic Pt^0 is present, thus confirming the generation of PdNPs on RubNRs. Based on the above analysis results, we concluded that PtNPs@RubNRs were successfully synthesized.

Next, the ECL intensity and stability of the PtNPs@RubNRs were tested (Figure 1D). After 15 consecutive scanning cycles, there was no significant fluctuation in ECL intensity (average intensity, 15016.3 au; relative standard deviation, 2.17%). Thus, PtNPs@RubNRs exhibit strong ECL intensity and excellent ECL stability.

Possible ECL Mechanism of the PtNPs@RubNRs. To investigate the ECL mechanism of PtNPs@RubNRs, a series of controlled experiments were designed. As shown in Figure 2, the ECL signal and its corresponding CV curves were measured under a potential scan from −0.9 to 1.1 V. In PBS solution at pH 7.4, the ECL signal of RubNRs was weak (1263 au) and there was no obvious redox peak (Figure 2A−C, curve a). These results reflect the low rate of generation of reactive oxygen species (ROS) from dissolved O_2 in solution. Next, the RubNRs modified electrode was scanned in PBS containing 320 mM H_2O_2 (Figure 2A−C, curve b). The ECL signal (7225 au) was enhanced because H_2O_2 produces ROS (such as $O_2^{\bullet-}$ and $OH^{\bullet}$) at a faster rate than dissolved O_2. These ROS act as intermediates that react with RubNRs to promote its ECL signal. Using modified electrodes decorated with PtNPs@RubNRs, the ECL signal measured in PBS solution was enhanced to 15016.3 au (11.9 times stronger than the signal obtained using RubNRs without PtNPs). In addition, the CV curve exhibited a reduction peak with a high current at −0.71 V[58] (Figure 2A−C, curve c), and this was attributed to the reduction peak of O_2. Hence, PtNPs promote the reduction of dissolved O_2 to generate more ROS to interact with $Rub^{\bullet+}$, thus improving the efficiency of the ECL reaction.

To explore the effects of ROS ($O_2^{\bullet-}$ and $OH^{\bullet}$) on the ECL reaction, L-cysteine was used as a scavenger of $O_2^{\bullet-}$ and $OH^{\bullet}$,[51] Na_2SO_3 was used as a scavenger of $O_2^{\bullet-}$, and DMSO was used as a scavenger of $OH^{\bullet}$.[59] In PBS solution containing 1 mM L-cysteine, the ECL signal of PtNPs@RubNRs was almost completely quenched (124 au) (Figure 2A−C, curve d). In PBS solution containing 1 mM Na_2SO_3, the ECL signal was decreased to 404 au (Figure 2A−C, curve e). In comparison, DMSO only reduced the ECL signal of PtNPs@RubNRs in PBS to 1717 au (Figure 2A−C, curve f). These results indicate that both the aqueous $O_2^{\bullet-}$ and $OH^{\bullet}$ can react with $Rub^{\bullet+}$ to form excited state substances (Rub*), with the aqueous $O_2^{\bullet-}$ playing the greater role. A plausible ECL enhancement mechanism is described as the following equations:

$$O_2 + e^- \xrightarrow{\text{PtNPs}} O_2^{\bullet-} \quad (1)$$

$$O_2 + 2H_2O + 2e^- \xrightarrow{\text{PtNPs}} H_2O_2 + 2OH^- \quad (2)$$

$$O_2^{\bullet-} + H_2O_2 \rightarrow O_2 + OH^- + OH^{\bullet} \quad (3)$$

$$Rub - e^- \rightarrow Rub^{\bullet+} \quad (4)$$

$$Rub^{\bullet+} + O_2^{\bullet-} \rightarrow Rub^* + O_2 \quad (5)$$

$$Rub^{\bullet+} + OH^{\bullet} \rightarrow Rub^* + OH^- \quad (6)$$

$$Rub^* \rightarrow Rub + h\nu \quad (7)$$

Optimization of Reaction Conditions. To obtain the optimal reaction conditions, several important experimental parameters were varied (including the concentration and

https://doi.org/10.1021/acs.analchem.3c05766
Anal. Chem. 2024, 96, 3636−3644

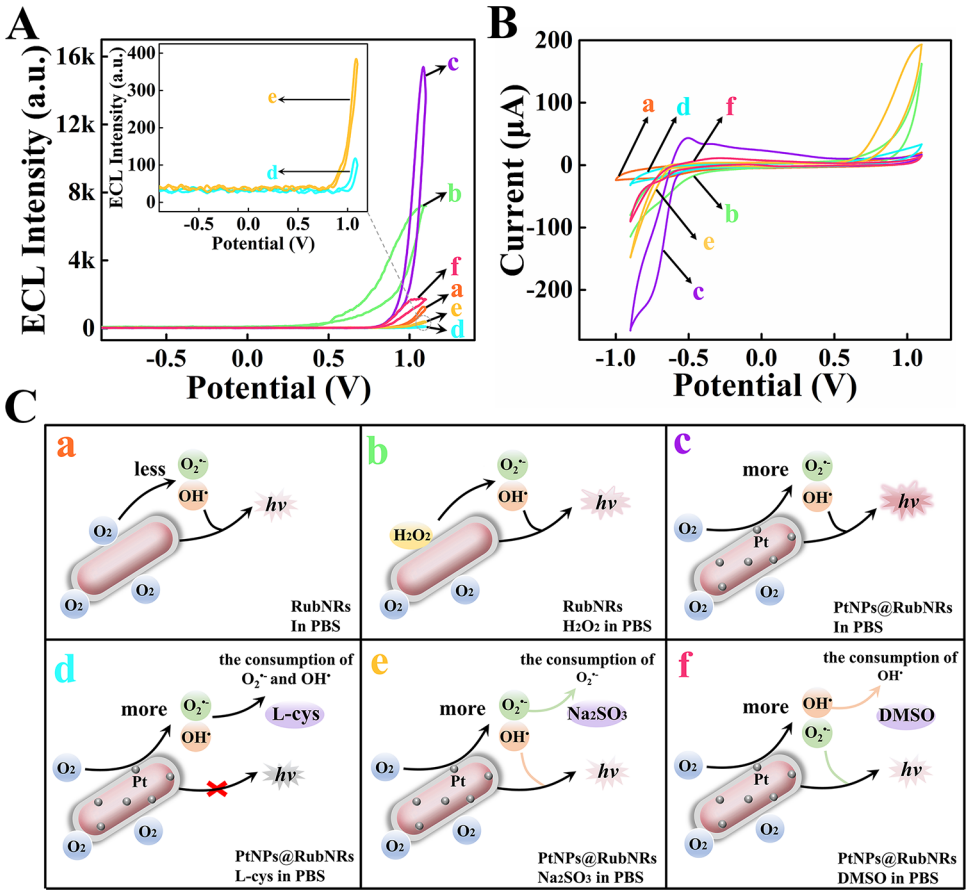

Figure 2. ECL mechanism of PtNPs@RubNRs. (A) ECL-potential profiles, (B) CV curves, and (C) possible ECL mechanisms for the following electrodes: RubNRs in PBS solution (curve a); RubNRs in PBS solution + 320 mM H_2O_2 (curve b); PtNPs@RubNRs in PBS solution (curve c); PtNPs@RubNRs in PBS solution + 1 mM L-cysteine (curve d); PtNPs@RubNRs in PBS solution + 1 mM Na_2SO_3 (curve e); and PtNPs@RubNRs in PBS solution containing 10 μL of DMSO (curve f).

incubation time). First, we optimized the concentration of the Y-shaped DNA structure (that quenches the ECL signal to detect miR-21) and its reaction time incubated on the electrode. As shown in Figure 3A, as the concentration of the Y-shaped structure increased, the ECL response gradually decreased, and the rate of decrease slowed when the Y-shaped structure concentration exceeded 2 μM. Thus, the optimum concentration of the Y-shaped structure was 2 μM. The incubation time for the Y-shaped structure was measured from 30 to 180 min. The ECL signal gradually decreased, with a slow rate of decrease after 120 min (Figure 3B). Therefore, 120 min was chosen as the optimum reaction time for the Y-shaped structure to incubate on the electrode.

MiR-105 binding causes the S strand to detach from L−S−T, and the free S can squeeze out the Y-shaped structure, ultimately leading to the recovery of the ECL signal during miR-105 detection. Hence, it is also necessary to optimize both the concentration of L−S−T and the time for S incubation on the electrode. As shown in Figure 3C, the ECL signal gradually increased as the concentration of L−S−T (the concentration of S) increased from 1 to 4 μM, reaching a plateau at 3 μM. Therefore, the optimal concentration of L−S−T was 3 μM. The ECL signal increased rapidly before 100 min and then slowed (Figure 3D). Thus, 100 min was used as the incubation time for S during subsequent experiments.

Analytical Performance of the Proposed ECL Biosensor for miR-21 Quantification. Using the above

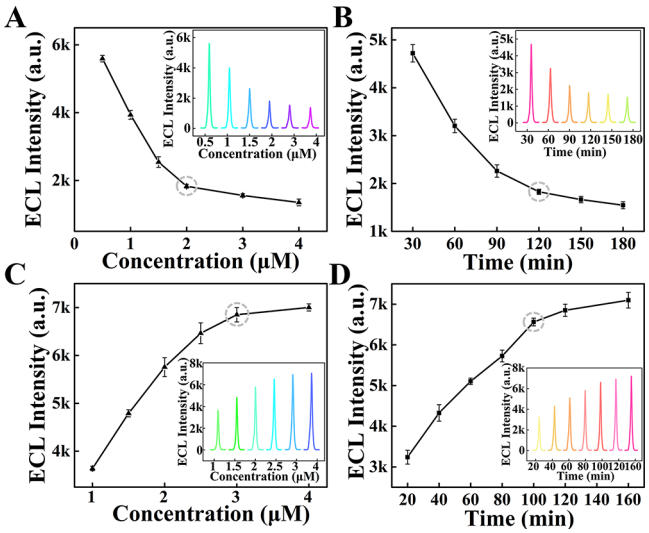

Figure 3. Optimization of the reaction conditions. Optimization of (A) the concentration of Y-shaped structures, (B) their reaction time on the electrode, (C) the concentration of L−S−T (the concentration of S), and (D) the incubation time of S on the electrode.

optimized conditions, the proposed ECL biosensor was employed to quantitatively detect different concentrations of miR-21 in the "on−off" mode. Figure 4A,B demonstrates that the ECL intensity gradually decreased as the concentration of

https://doi.org/10.1021/acs.analchem.3c05766
Anal. Chem. 2024, 96, 3636−3644

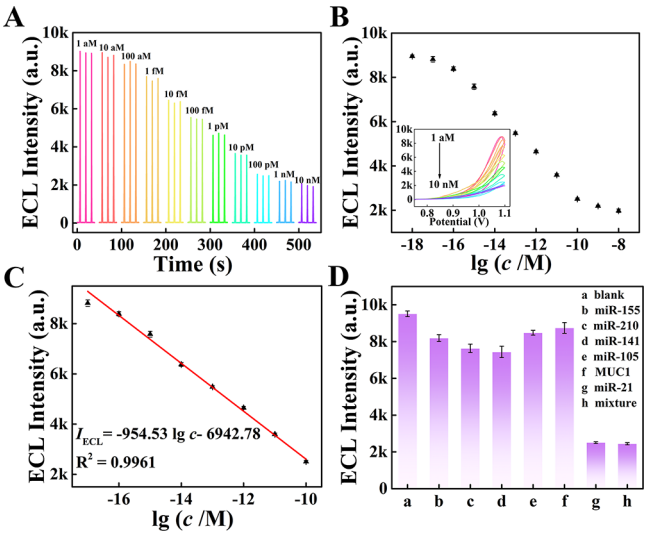

Figure 4. Analytical performance for miR-21 quantification. (A) Stability of the proposed biosensor in various concentrations of miR-21 (1 aM, 10 aM, 100 aM, 1 fM, 10 fM, 100 fM, 1 pM, 10 pM, 100 pM, 1 nM, and 10 nM). (B) Scatter plot of ECL intensity−time (inset of the ECL intensity−potential plot). (C) Calibration curve showing the relationship between the ECL intensity and the logarithm of miR-21 concentration (n = 3). (D) Selectivity of the proposed ECL biosensor for several interfering molecules.

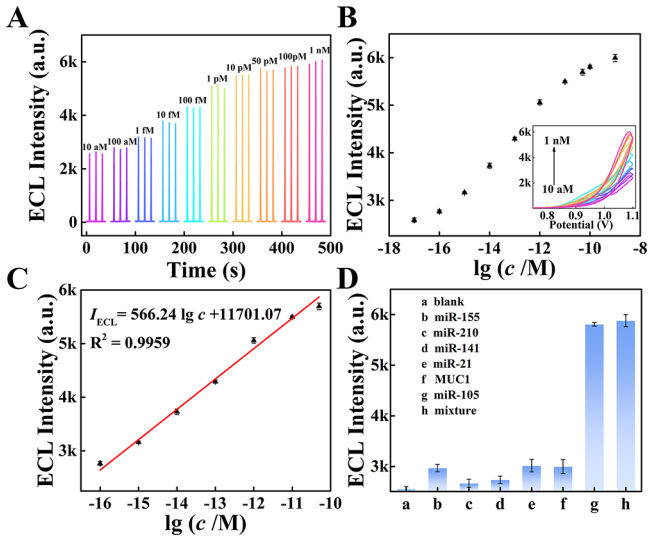

Figure 5. Analytical performance for miR-105 quantification. (A) Stability of the proposed biosensor with different concentrations of miR-105 (10 aM, 100 aM, 1 fM, 10 fM, 100 fM, 1 pM, 10 pM, 50 pM, 100 pM, and 1 nM). (B) Scatter plot of ECL intensity−time (inset, ECL intensity−potential plot). (C) Calibration curve of the relationship between the ECL intensity and the logarithm of miR-105 concentration (n = 3). (D) Selectivity of the proposed ECL biosensor for several interfering molecules.

miR-21 increased from 1 aM to 10 nM. Moreover, the stability of the ECL intensity corresponding to each concentration was excellent after three consecutive scanning cycles. A scatter plot of ECL intensity−time (with an intensity−potential plot inset) is shown in Figure 4B. The consequent calibration plot exhibited a satisfactory linear relationship between ECL intensity (I) and the logarithmic values of miR-21 concentration (lg c) in the 10 aM to 100 pM range (Figure 4C). This calibration plot yielded a correlation coefficient of 0.9961, and the linear regression equation was I_{ECL} = −954.53 lg c −6942.78. The limit of detection (LOD) was calculated to be 2.03 aM by using the 3σ method (S/N = 3).

To verify the selectivity of the proposed ECL biosensor, several relevant interfering molecules, including miR-155, miR-210, miR-141, miR-105, and MUC1 (at an identical concentration of 1 nM), were employed for comparison to miR-21 (100 pM). As shown clearly in Figure 4D, the ECL signal was significantly quenched only in the presence of miR-21 (including a mixture containing miR-21). Because miR-21-induced quenching was markedly larger than quenching with interfering factors, we conclude that the designed biosensor can achieve the specific detection of miR-21.

Analytical Performance of the Proposed ECL Biosensor for miR-105 Quantification. We next evaluated the quantitative detection of miR-105 using the proposed ECL biosensor. To achieve quantitative detection of miR-105, 100 pM miR-21 was initially added to the biosensor to quench the ECL signal. The detection results are shown in Figure 5A (for the 10 aM to 1 nM concentration range). The ECL intensity at various concentrations was observed to exhibit good stability. The ECL intensity−time scatter plot and intensity−potential plot (inset) are shown in Figure 5B. The ECL intensity demonstrated a good linear correlation with the logarithm of the miR-105 concentration. The consequent calibration curve is shown in Figure 5C, and the linear regression equation was expressed as I_{ECL} = 566.24 lg c + 11701.07 with a correlation coefficient of 0.9959. The LOD was calculated to be 80.4 aM.

To investigate the selectivity of the biosensor, potentially interfering miRNAs, including miR-155, miR-210, miR-141, miR-21, and MUC1 (all at 1 nM), were employed for comparison with miR-105 (100 pM; Figure 5D). Despite their higher concentration, the interfering molecules provoked very little ECL signal recovery. In contrast, the ECL intensity was elevated significantly in the presence of miR-105 (including a mixture containing miR-105), demonstrating that the biosensor possessed excellent selectivity.

Use of the Proposed ECL Biosensor for the Analysis of Different Cancer Cells and Breast Cancer Metastatic Cells. After validation of its performance, our biosensor was applied to the analysis of cancer cells. The biosensor was first used to distinguish breast cancer cell lines and then to differentiate the metastatic breast cancer cells among these breast cancer cell lines (Figure 6A). Total miRNAs were extracted separately from each group of cells using the TRIzol method (Supporting Information 1.4) for subsequent ECL testing. Figure 6B demonstrates the different degrees of quenching of ECL intensity caused by the different miR-21 levels in different cancer cell lines, i.e., HepG2 (liver cancer cells), TPC-1 (thyroid cancer cells), HeLa (cervical cancer cells), MCF-7 (breast cancer cells), and MDA-MB-231 (breast cancer cells). While statistical analysis revealed that miR-21 was expressed in all of these cancer cells, miR-21 expression levels in breast cancer cells were significantly higher (compared to other cancer cell lines). Thus, the biosensor can sensitively identify breast cancer cells.

Among the breast cancer cells screened, metastatic breast cancer cells can be readily distinguished through the miR-105-induced enhancement of the ECL signal. Figure 6C demonstrates the enhanced ECL signals obtained by using MCF-7 and MDA-MB-231 cells. As expected, miR-105 levels (and ECL signal intensity) were significantly higher in

https://doi.org/10.1021/acs.analchem.3c05766
Anal. Chem. 2024, 96, 3636−3644

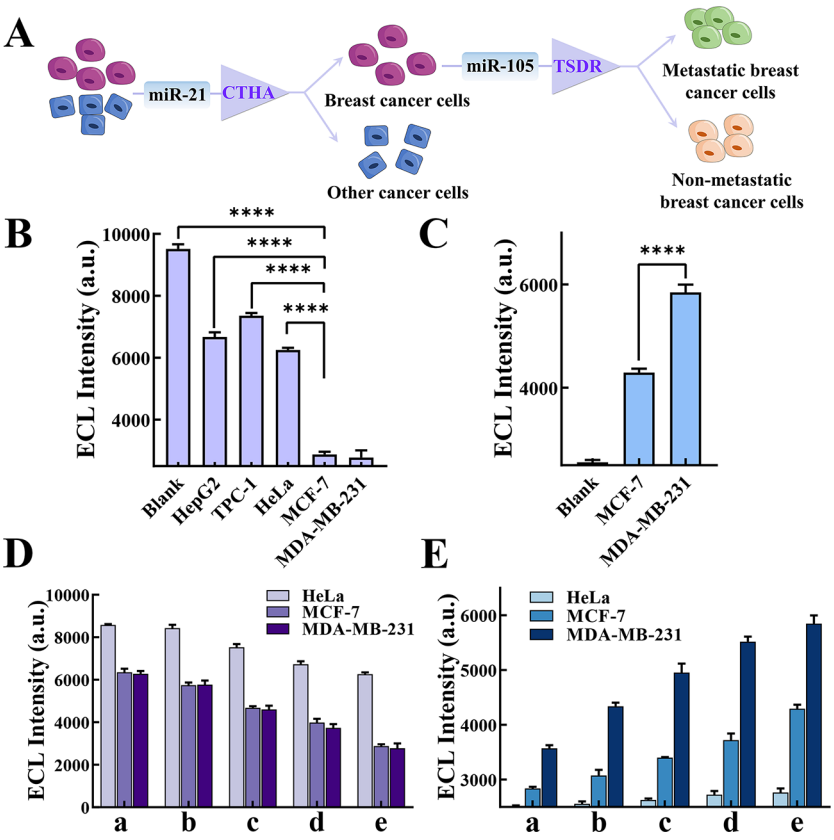

Figure 6. Analysis of cancer cells and breast cancer metastatic cells. (A) Schematic diagram of the application of the biosensor to the diagnosis of breast cancer and the identification of breast cancer metastasis. (B) Statistical analysis of ECL quenching by miR-21 in different cancer cells (HepG2, TPC-1, HeLa, MCF-7, and MDA-MB-231) (*t* test; ****, $p < 0.0001$). (C) Statistical analysis of ECL recovery with miR-105 in different breast cancer cells (MCF-7 and MDA-MB-231) (*t* test; ****, $p < 0.0001$). Detection of (D) miR-21 and (E) miR-105 in HeLa, MCF-7, and MDA-MB-231 cells with the proposed biosensor using different cell numbers: (a) 10, (b) 10^2, (c) 10^3, (d) 10^4, and (e) 10^5 cells.

metastatic MDA-MB-231 cells than in malignant MCF-7 cells. Together, these ECL results show that miR-21 levels can be used to distinguish breast cancer cells from other cancer cells and that miR-105 levels can be used to further identify the characteristics of breast cancer metastasis.

Figure 6D,E demonstrates how these ECL signals change across different cell lines with increasing cell numbers (from 10^1 to 10^5). For this comparison, we used HeLa, MCF-7, and MDA-MB-231 cells as the detection samples. The degree of quenching of ECL by miR-21 using different cell numbers is shown in Figure 6D. As the number of HeLa cells increased, the ECL signal decreased only slightly and the rate of decrease was slow. In contrast, an obvious decrease in the ECL signal was observed using MCF-7 and MDA-MB-231 cells. As shown in Figure 6E, there was a gradual increase in the ECL intensity (caused by miR-105) in both MCF-7 and MDA-MB-231 cells as the cell number increased. However, the increase observed using MDA-MB-231 cells was more marked, further confirming that miR-105 levels in MDA-MB-231 cells are much higher than those in MCF-7 cells. Importantly, the application of miR-105 to identify metastatic cells was sensitive even at low cell numbers. Measured miR-105 levels in HeLa cells remained extremely low. The above results indicate the great feasibility of the designed biosensor for identifying breast cancer and for determining whether the breast cancer has metastasized.

Use of the Proposed ECL Biosensor for the Analysis of Human Serum Samples. The applicability of the proposed biosensor to real human serum was evaluated using the standard addition method. First, different concentrations of miR-21 (100 aM, 100 fM, 1 pM, and 100 pM) were spiked into real serum samples from healthy individuals, and these were detected by the biosensor with recoveries of 94.6–101.1% (Table S4). After miR-21 was added at a constant concentration of 100 pM as a control, different concentrations of miR-105 (1 fM, 10 fM, 100 fM, and 1 pM) were spiked into human serum samples, with recovery rates from 90.4 to 106% (Table S5). The above results suggest that the biosensor developed has the potential to be applied to real human serum samples for the detection of both miRNAs.

To further examine the clinical diagnostic capability of the constructed biosensor, we extracted total miRNAs from healthy human serum and from metastatic breast cancer patient serum using the TRIzol method and then applied the proposed strategy to analyze miR-21 and miR-105 levels in serum (Figure 7). The results reveal that the degree of quenching of ECL caused by miR-21 and the degree of recovery of the ECL signal caused by miR-105 were significantly stronger in patients with breast cancer metastasis (compared with healthy human samples). These results provide evidence that our constructed biosensor for the detection of miR-21 and miR-105 levels in serum can readily distinguish breast cancer patients from healthy individuals. This is of great significance for the timely and accurate diagnosis of breast cancer.

https://doi.org/10.1021/acs.analchem.3c05766
Anal. Chem. 2024, 96, 3636−3644

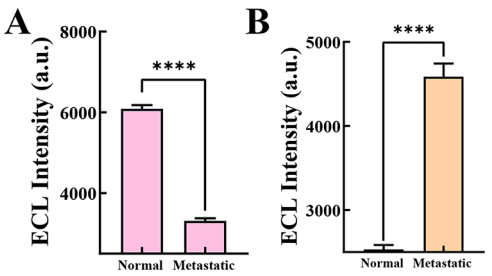

Figure 7. Analysis of the human serum samples. ECL response induced by (A) miR-21 and (B) miR-105 in the serum of healthy individuals and patients with breast cancer metastasis (*t* test; ****, $p < 0.0001$).

CONCLUSIONS

In summary, an "on−off−on" ECL biosensor based on two enzyme-free DNA amplification circuits was successfully constructed and applied to the accurate diagnosis of breast cancer and the recognition of metastasis through the detection of miR-21 and miR-105 levels, respectively. The biomarker miR-21 triggers the first CTHA amplification circuit, which ultimately produces the Fc-modified Y-shaped structures that can quench the ECL signal of the PtNPs@RubNRs, thus allowing the sensitive identification of breast cancer. Additionally, miR-105, a breast cancer metastasis biomarker, initiates the second TSDR amplification circuit that eventually recovers the above quenched ECL signal, thus determining the breast cancer metastasis. Our experimental results demonstrate that the ECL biosensor exhibits excellent performance for miR-21 and miR-105 detection and has been successfully applied to the analysis of cells and serum. We expect that the designed biosensor will provide a reliable method for accurate breast cancer screening. MiRNAs have an important impact in cancer development and progression; therefore, in the subsequent study, more miRNAs biomarkers assays can be combined with ECL biosensors to achieve more sensitive and accurate clinical analysis and diagnosis.

ASSOCIATED CONTENT

Supporting Information

The Supporting Information is available free of charge at https://pubs.acs.org/doi/10.1021/acs.analchem.3c05766.

Additional experimental details including reagents, apparatus, sequence information for the DNA oligonucleotides, theoretical simulation of DNA amplification circuits using NUPACK, steps for total miRNAs extraction, characterization of PtNPs@RubNRs, polyacrylamide gel electrophoresis analysis, characterization of the modified electrode, detection limit, supplementary figures, supplementary tables, and references (PDF)

AUTHOR INFORMATION

Corresponding Authors

Pinyi Ma − *College of Chemistry, Jilin Province Research Center for Engineering and Technology of Spectral Analytical Instruments, Jilin University, Changchun 130012, China;* orcid.org/0000-0002-3230-4928; Email: mapinyi@jlu.edu.cn

Daqian Song − *College of Chemistry, Jilin Province Research Center for Engineering and Technology of Spectral Analytical Instruments, Jilin University, Changchun 130012, China;* orcid.org/0000-0002-4866-1292; Email: songdq@jlu.edu.cn

Authors

Zhuoxin Ye − *College of Chemistry, Jilin Province Research Center for Engineering and Technology of Spectral Analytical Instruments, Jilin University, Changchun 130012, China*

Mo Ma − *College of Chemistry, Jilin Province Research Center for Engineering and Technology of Spectral Analytical Instruments and School of Pharmacy, Jilin University, Changchun 130012, China*

Yuxuan Chen − *College of Chemistry, Jilin Province Research Center for Engineering and Technology of Spectral Analytical Instruments, Jilin University, Changchun 130012, China*

Ruiyan Liu − *College of Chemistry, Jilin Province Research Center for Engineering and Technology of Spectral Analytical Instruments, Jilin University, Changchun 130012, China*

Yan Zhang − *College of Chemistry, Jilin Province Research Center for Engineering and Technology of Spectral Analytical Instruments, Jilin University, Changchun 130012, China*

Complete contact information is available at: https://pubs.acs.org/10.1021/acs.analchem.3c05766

Author Contributions

Z.Y.: conceptualization, data curation, formal analysis, investigation, and writing (original draft). M.M.: data curation and biological experiments. Y.C.: literature summary and investigation. R.L.: formal analysis and investigation. Y.Z.: data curation and investigation. P.M.: conceptualization, project administration, data curation, and writing (review and editing). D.S.: project administration, funding acquisition, resources, and supervision.

Notes

The authors declare no competing financial interest.

ACKNOWLEDGMENTS

This work was supported by the National Natural Science Foundation of China (22074052 and 22004046) and the Science and Technology Developing Foundation of Jilin Province of China (20230101033JC, 20220505015ZP, and YDZJ202302CXJD031).

REFERENCES

(1) Gao, G.; Jiang, Y.-W.; Zhan, W.; Liu, X.; Tang, R.; Sun, X.; Deng, Y.; Xu, L.; Liang, G. *J. Am. Chem. Soc.* **2022**, *144*, 11897−11910.
(2) Valastyan, S.; Weinberg, R. A. *Cell* **2011**, *147*, 275−292.
(3) Cao, Y.; Yu, X.; Zeng, T.; Fu, Z.; Zhao, Y.; Nie, B.; Zhao, J.; Yin, Y.; Li, G. *J. Am. Chem. Soc.* **2022**, *144*, 13475−13486.
(4) Chaffer, C. L.; Weinberg, R. A. *Science* **2011**, *331*, 1559−1564.
(5) Rubens, R. D. *Int. J. Clin. Pract.* **2001**, *55*, 676−679.
(6) Ye, H.; Wang, K.; Lu, Q.; Zhao, J.; Wang, M.; Kan, Q.; Zhang, H.; Wang, Y.; He, Z.; Sun, J. *Biomaterials* **2020**, *242*, No. 119932.
(7) Mitchell, P. S.; Parkin, R. K.; Kroh, E. M.; Fritz, B. R.; Wyman, S. K.; Pogosova-Agadjanyan, E. L.; Peterson, A.; Noteboom, J.; O'Briant, K. C.; Allen, A.; Lin, D. W.; Urban, N.; Drescher, C. W.; Knudsen, B. S.; Stirewalt, D. L.; Gentleman, R.; Vessella, R. L.; Nelson, P. S.; Martin, D. B.; Tewari, M. *Proc. Natl. Acad. Sci. U.S.A.* **2008**, *105*, 10513−10518.
(8) Wang, Z.-y.; Li, D.-l.; Tian, X.; Zhang, C.-y. *Chem. Sci.* **2021**, *12*, 10426−10435.
(9) Zhou, J.; Peng, X.; Yang, Z.; Zhuo, Y.; Liang, W.; Yuan, R.; Chai, Y. *Anal. Chem.* **2022**, *94*, 9911−9918.
(10) Lokody, I. *Nat. Rev. Genet.* **2014**, *15*, 362−362.

(11) Zhou, W.; Fong, M. Y.; Min, Y.; Somlo, G.; Liu, L.; Palomares, M. R.; Yu, Y.; Chow, A.; O'Connor, S. T. F.; Chin, A. R.; Yen, Y.; Wang, Y.; Marcusson, E. G.; Chu, P.; Wu, J.; Wu, X.; Li, A. X.; Li, Z.; Gao, H.; Ren, X.; Boldin, M. P.; Lin, P. C.; Wang, S. E. *Cancer Cell* **2014**, *25*, 501−515.
(12) Chen, H.; Liu, Y.; Feng, S.; Cao, Y.; Wu, T.; Liu, Z. *Biosens. Bioelectron.* **2022**, *200*, No. 113913.
(13) Song, C.; Liu, C.; Chen, J.; Ma, Z.; Tang, S.; Pan, R.; Suo, X.; Yan, Z.; Lee, H. K.; Shen, W. *Anal. Chem.* **2023**, *95*, 4113−4121.
(14) Yan, H. H.; Huang, M.; Zhu, F.; Cheng, R.; Wen, S.; Li, L. T.; Liu, H.; Zhao, X. H.; Luo, F. K.; Huang, C. Z.; Wang, J. *Anal. Chem.* **2023**, *95*, 3968−3975.
(15) Li, R.; Li, F.; Zhang, Y.; He, Y.; Wang, Y.; Wang, F. *Anal. Chem.* **2023**, *95*, 3848−3855.
(16) Li, J.; Liu, J.; Bi, Y.; Sun, M.; Bai, J.; Zhou, M. *Anal. Chim. Acta* **2020**, *1105*, 87−94.
(17) Wu, L.; Qu, X. *Chem. Soc. Rev.* **2015**, *44*, 2963−2997.
(18) Duan, R.; Zuo, X.; Wang, S.; Quan, X.; Chen, D.; Chen, Z.; Jiang, L.; Fan, C.; Xia, F. *J. Am. Chem. Soc.* **2013**, *135*, 4604−4607.
(19) Pinto, R.; Pilato, B.; Ottini, L.; Lambo, R.; Simone, G.; Paradiso, A.; Tommasi, S. *J. Cell Physiol.* **2013**, *228*, 1264−1269.
(20) Yang, L.; Yu, S.; Yan, Y.; Bi, S.; Zhu, J.-J. *Anal. Chem.* **2022**, *94*, 7075−7083.
(21) Zhu, L.; Yu, L.; Yang, X. *Anal. Chem.* **2022**, *94*, 17279−17286.
(22) Yang, W.; Shen, Y.; Zhang, D.; Li, C.; Yuan, R.; Xu, W. *Anal. Chem.* **2019**, *91*, 7782−7789.
(23) Xu, S.; Chang, Y.; Wu, Z.; Li, Y.; Yuan, R.; Chai, Y. *Biosens. Bioelectron.* **2020**, *149*, No. 111848.
(24) Han, F.; Jiang, H.; Fang, D.; Jiang, D. *Anal. Chem.* **2014**, *86*, 6896−6902.
(25) Zhang, P.; Lin, Z.; Zhuo, Y.; Yuan, R.; Chai, Y. *Anal. Chem.* **2017**, *89*, 1338−1345.
(26) Peng, L.; Zhang, P.; Chai, Y.; Yuan, R. *Anal. Chem.* **2017**, *89*, 5036−5042.
(27) Chen, F.; Li, G.; Wu, C.; Wang, L.; Ko, C.-N.; Ma, D.-L.; Leung, C.-H. *Anal. Chem.* **2022**, *94*, 4513−4521.
(28) Su, J.; Du, J.; Ge, R.; Sun, C.; Qiao, Y.; Wei, W.; Pang, X.; Zhang, Y.; Lu, H.; Dong, H. *Anal. Chem.* **2022**, *94*, 13108−13116.
(29) Wang, Q.; Liu, Y.; Wang, X.; Wang, F.; Zhang, L.; Ge, S.; Yu, J. *ACS Appl. Mater. Interfaces* **2021**, *13*, 25783−25791.
(30) Han, T.; Ma, C.; Wang, L.; Cao, Y.; Chen, H. Y.; Zhu, J. J. *Adv. Funct. Mater.* **2022**, *32*, 2200863.
(31) Sun, W.; Zhang, N.; Ren, X.; Wu, D.; Jia, Y.; Wei, Q.; Ju, H. *Biosens. Bioelectron.* **2023**, *242*, No. 115750.
(32) Wei, X.; Zhu, M. J.; Cheng, Z.; Lee, M.; Yan, H.; Lu, C.; Xu, J. J. *Angew. Chem., Int. Ed.* **2019**, *58*, 3162−3166.
(33) Xiong, X.; Xiong, C.; Gao, Y.; Xiao, Y.; Chen, M.-M.; Wen, W.; Zhang, X.; Wang, S. *Anal. Chem.* **2022**, *94*, 7861−7867.
(34) Shu, W.-Y.; Su, R.; Yao, L.; Xiao, Y.; Chen, M.-M.; Wen, W.; Wang, S.; Xiong, C.; Zhang, X. *Adv. Sensor Energy Mater.* **2023**, *2*, No. 100059.
(35) Wang, F.; Liu, Y.; Fu, C.; Li, N.; Du, M.; Zhang, L.; Ge, S.; Yu, J. *Anal. Chem.* **2021**, *93*, 1702−1708.
(36) Gao, C.; Yu, H.; Wang, Y.; Liu, D.; Wen, T.; Zhang, L.; Ge, S.; Yu, J. *Anal. Chem.* **2020**, *92*, 6822−6826.
(37) Bao, Y.; Jiang, Y.; Xiong, E.; Tian, T.; Zhang, Z.; Lv, J.; Li, Y.; Zhou, X. *ACS Sens.* **2020**, *5*, 1082−1091.
(38) Egloff, S.; Melnychuk, N.; Reisch, A.; Martin, S.; Klymchenko, A. S. *Biosens. Bioelectron.* **2021**, *179*, No. 113084.
(39) Zhang, X.; Zhou, Y.; Chai, Y.; Yuan, R. *Anal. Chem.* **2021**, *93*, 7987−7992.
(40) Zhang, X.-L.; Yin, Y.; Du, S.-M.; Kong, L.-Q.; Chai, Y.-Q.; Li, Z.-H.; Yuan, R. *Anal. Chem.* **2021**, *93*, 13952−13959.
(41) Li, C.; Zhang, J.; Gao, Y.; Luo, S.; Wu, Z.-S. *ACS Sens.* **2022**, *7*, 601−611.
(42) Li, R.; Zhu, Y.; Gong, X.; Zhang, Y.; Hong, C.; Wan, Y.; Liu, X.; Wang, F. *J. Am. Chem. Soc.* **2023**, *145*, 2999−3007.
(43) Wan, Y.; Li, G.; Zou, L.; Wang, H.; Wang, Q.; Tan, K.; Liu, X.; Wang, F. *Anal. Chem.* **2021**, *93*, 11052−11059.
(44) Luo, J.-H.; Li, Q.; Chen, S.-H.; Yuan, R. *ACS Appl. Mater. Interfaces* **2019**, *11*, 27363−27370.
(45) Lv, Y.; Cui, L.; Peng, R.; Zhao, Z.; Qiu, L.; Chen, H.; Jin, C.; Zhang, X.-B.; Tan, W. *Anal. Chem.* **2015**, *87*, 11714−11720.
(46) Yu, L.; Zhu, L.; Yan, M.; Feng, S.; Huang, J.; Yang, X. *Anal. Chem.* **2021**, *93*, 11809−11815.
(47) Miao, P.; Tang, Y. *CCS Chem.* **2021**, *3*, 2331−2339.
(48) Li, X.-R.; Wang, L.; Liang, W.-B.; Yuan, R.; Zhuo, Y. *Anal. Chem.* **2022**, *94*, 3313−3319.
(49) Liu, J.-L.; Tang, Z.-L.; Zhang, J.-Q.; Chai, Y.-Q.; Zhuo, Y.; Yuan, R. *Anal. Chem.* **2018**, *90*, 5298−5305.
(50) Song, Y.; Tao, X.; Liang, W.; Zhong, X.; Yuan, R.; Zhuo, Y. *Chin. Chem. Lett.* **2023**, *34*, No. 107957.
(51) Liu, J.-L.; Tang, Z.-L.; Zhuo, Y.; Chai, Y.-Q.; Yuan, R. *Anal. Chem.* **2017**, *89*, 9108−9115.
(52) Wu, J.; Ran, P.; Zhu, S.; Mo, F.; Wang, C.; Fu, Y. *Sens. Actuators B Chem.* **2019**, *278*, 97−102.
(53) Wang, L.; Liu, P.; Liu, Z.; Zhao, K.; Ye, S.; Liang, G.; Zhu, J.-J. *ACS Sens.* **2020**, *5*, 3584−3590.
(54) Chen, A.; Ma, S.; Zhuo, Y.; Chai, Y.; Yuan, R. *Anal. Chem.* **2016**, *88*, 3203−3210.
(55) Lu, J.; Wang, J.; Hu, X.; Gyimah, E.; Yakubu, S.; Wang, K.; Wu, X.; Zhang, Z. *Anal. Chem.* **2019**, *91*, 7353−7359.
(56) Cao, W.; Ferrance, J. P.; Demas, J.; Landers, J. P. *J. Am. Chem. Soc.* **2006**, *128*, 7572−7578.
(57) Pan, M.-C.; Gao, M.-H.; Yang, X.; Liang, W.-B.; Yuan, R.; Zhuo, Y. *ACS Sens.* **2022**, *7*, 2475−2482.
(58) Yang, S.-S.; Jiang, M.-H.; Chai, Y.-Q.; Yuan, R.; Zhuo, Y. *ACS Appl. Mater. Interfaces* **2018**, *10*, 38648−38655.
(59) Tao, X.-L.; Pan, M.-C.; Yang, X.; Yuan, R.; Zhuo, Y. *Chin. Chem. Lett.* **2022**, *33*, 4803−4807.

https://doi.org/10.1021/acs.analchem.3c05766
Anal. Chem. 2024, 96, 3636−3644